A Journal of the Gesellschaft Deutscher Chemiker

Angewandte International Edition GDCh Chemie

www.angewandte.org

Accepted Article

Title: Creation of dopant-plasmon synergism in double perovskites for bias-free photoelectrochemical synthesis of bromohydrins and hydrogen peroxide

Authors: Linqian Li, Qiang Luo, Yifan Wang, Xueli Zhang, Yating Wen, Ning Wang, Thamraa AlShahrani, and Shengqian Ma

To be cited as: *Angew. Chem. Int. Ed.* **2025**, e202424395

Link to VoR: https://doi.org/10.1002/anie.202424395

WILEY VCH

10.1002/anie.202424395

WILEY VCH

RESEARCH ARTICLE

Creation of Dopant-Plasmon Synergism in Double Perovskites for Bias-free Photoelectrochemical Synthesis of Bromohydrins and Hydrogen Peroxide

Linqian Li[a], Qiang Luo* [a], Yifan Wang[a], Xueli Zhang[a], Yating Wen[a], Ning Wang* [a], Thamraa AlShahrani,[c] Shengqian Ma* [b]

[a] L. Li, Prof. Q. Luo, S. Chen, Y. Wang, X. Zhang, Y. Wen, Y. Yang, Prof. N. Wang
State Key Laboratory of Marine Resource Utilization in South China Sea, Hainan University, Haikou, 570228, P. R. China
E-mail: luo-q11@foxmail.com; wangn02@foxmail.com

[b] Prof. S. Ma
Department of Chemistry, University of North Texas, Denton, TX, 76201 USA
E-mail: Shengqian.Ma@unt.edu

[c] Prof. T. AlShahrani
Department of Physics, College of Science, Princess Nourah bint Abdulrahman University, Riyadh 11564, Saudi Arabia

Supporting information for this article is given via a link at the end of the document.

Abstract: The integration of photoexcited charge carriers into the synthesis of valuable chemicals offers substantial sustainability benefits, particularly by replacing toxic and costly oxidants and reductants typically used in conventional processes. The efficiency of such transformations is fundamentally governed by the ability to optimize light absorption and charge carrier dynamics within photoelectrodes/photocatalysts. Herein, we present a Cu^{+}/Cu^{2+}-substituted double perovskite $Cs_2AgBiBr_6$ photoanode, embedded with plasmonic Ag nanoparticles, for bias-free photoelectrochemical production of bromohydrins and H_2O_2. Spectroscopic analyses, coupled with three-dimensional finite-difference time-domain simulations, demonstrate that the inclusion of Ag nanoparticles significantly enhances electromagnetic energy utilization and improves carrier separation efficiency. The synergistic effect of the Cu^{2+} and Ag nanoparticles results in a 7-fold increase in the yield of 2-bromo-1-phenylethanol, compared to pristine $Cs_2AgBiBr_6$, alongside an impressive H_2O_2 productivity of 25.8 μmol h^{-1} cm^{-2}. Experimental and theoretical investigations reveal that the Cu^{2+} substitution strengthens Br^- adsorption and oxidation, promoting the bromohydroxylation of alkenes via electrophilic addition in the bulk solution. These findings offer critical insights into the design of advanced metal halide perovskites for sustainable and solar-driven chemical transformations.

Introduction

Upgrading low-cost chemicals to more valuable products play a meaningful role in advancing both chemical and pharmaceutical fields.[1] Halohydrins, as valuable building blocks, are critical in the synthesis of fine chemicals and pharmaceuticals, including epoxides, azidoalcohols, aminoalcohols, and aziridines.[2] Traditionally, halohydrins are synthesized via homogeneous catalytic halohydroxylation of alkenes, which involves reactive C=C bonds.[3] The demand for harsh reaction conditions and hazardous halogenating agents (i.e., Cl_2, Br_2, CH_2Cl_2, *N*-halosuccinimide) requires strict safety regulations and environmental preservation.[4] Alternatively, halohydrin production can be achieved through heterogeneous biocatalytic or electrochemical methods with the use of H_2O_2 and inorganic halide as reagents.[5] Despite the potential of these approaches, their widespread application is hindered by challenges such as the high cost of strong oxidants, uncontrolled over-oxidation, and the difficulty of purification. On the other hand, hydrogen peroxide (H_2O_2), an important and environmentally benign oxidant, is widely used in many important industrial processes, including pharmaceutical synthesis and environmental remediation.[6] Its high energy density also positions H_2O_2 as a promising clean energy intermediate and carrier. Conventionally, the anthraquinone process for selective H_2O_2 production needs high energy consumption and fossil-fuel derived H_2 feedstock at a high temperature and yields a lot of chemical wastes, undermining its sustainability.[7] Thus, it is imperative to develop green approaches for sustainable H_2O_2 production, avoiding the reliance on H_2 and minimizing capital and operational costs.

Photoelectrochemical strategy, leveraging energetic oxidative and reductive charges to drive chemical transformations, possess prominent advantages over conventional synthetic approaches by offering a milder and more efficient alternative to the use of hazardous or costly chemical oxidants/reductants.[8,9] Therefore, the concurrent production of halohydrins and H_2O_2 by direct solar energy conversion in a photoelectrochemical system without additional energy input is of great practical interest, which urges the search of highly active and robust photoanodes. Of the potential photoactive materials, metal halide perovskites have attracted an increasing attention for photochemical transformations owing to their fascinating photophysical characteristics and the power of easy modulation through ion substitution.[10] Nevertheless, traditional organic-inorganic hybrid perovskites suffer from two formidable challenges: the toxicity of lead and intrinsic instability of organic component in aqueous environments.[11] A promising strategy to address these limitations

10.1002/anie.202424395

involves the substitution of organic cations with cesium (Cs^+), which enhances the perovskite's decomposition energy and stability.[12] Furthermore, substituting Pb^{2+} with alternative metal ions such as silver (Ag^+) and bismuth (Bi^{3+}) can mitigate lead toxicity while simultaneously improving the material's Coulomb interaction and overall stability.[13] Unfortunately, $Cs_2AgBiBr_6$ suffers from a weak visible-light absorption and a severe charge recombination, leading to a very low photocatalytic activity.[14] This dilemma will be even further amplified in an unbiased photochemical cell due to the inefficient extraction of a significant fraction of photoexcited charge carriers. In this regard, substitution doping could be particularly promising in metal halide double perovskites for modulating their optoelectronic properties and catalytic activity.[15] For example, the partial substitution of Ag^+ with metal ions (e.g., Cu^+, Fe^{2+}, Sn^{4+}, and Ge^{4+}) results in the enhancement of absorption and photoconductivity of $Cs_2AgBiBr_6$.[16] In addition, the localized surface plasmon resonance (LSPR) induced by metal nanostructures has been considered as a reliable strategy to enhance the catalytic ability of a semiconductor.[17] In fact, several prominent advantages can be obtained by employing plasmon-enhanced light-matter interactions, including complementary light absorption, hot electron injection, junction-driven charge separation, and plasmon-induced resonance energy transfer.[18] However, conventional plasmonic enhancement techniques, which rely on the deposition of metal nanostructures on the semiconductor surface, often suffer from limited efficiency. To address this, the design of intimate metal-semiconductor heterostructures, in which metal nanoparticles are embedded within the semiconductor matrix, is increasingly preferred. This configuration maximizes the interaction between the metal and semiconductor, enhancing the material's ability to absorb electromagnetic energy and improve overall photoconversion efficiency.

Herein, we present the design and development of a novel inorganic double perovskite photoanode, $Cs_2AgCuBiBr_6$@Ag (denoted CACBB@Ag), for bias-free photoelectrochemical coupling synthesis of bromohydrins and H_2O_2. The photoanode integrates two advanced strategies: partial substitution of Ag^+ by Cu^+/Cu^{2+} and the embedding of plasmonic Ag nanoparticles within the perovskite matrix. This approach leverages the unique properties of both the perovskite and the plasmonic metal to enhance the photocatalytic performance. Comprehensive characterization through surface photovoltage spectroscopy, time-resolved transient absorption spectra, and three-dimensional finite-difference time-domain simulation reveals that the spatial confinement of Ag nanoparticles within the perovskite optimizes plasmonic energy utilization and extends the carrier lifetime. CACBB@Ag enables a high synthesis yield of bromohydrins with wide substrate scope and a high H_2O_2 production rate of 25.8 μmol h^{-1} cm^{-2}, outperforming the pristine perovskite. Density functional theory (DFT) studies verify that the concomitant Cu^{2+} substitution promotes the adsorption and catalytic oxidation of Br^-, which subsequently facilitates bromohydroxylation of organic molecules bearing C=C bonds by the electrophilic addition in the bulk solution.

Results and Discussion

Synthesis and characterization

A facile two-step synthesis strategy was developed for the construction of CACBB@Ag. First, $Cs_2AgCuBiBr_6$ (CACBB) was prepared through the reaction of CsBr, AgBr, $CuBr_2$ and $BiBr_3$. Then, a precursor solution was obtained by dissolving the resulting CACBB sample into dimethylformamide and dimethyl sulfoxide solvent (volume ratio 1:1). Next, the dispersion of Ag nanoparticles (~15 nm) was injected into the precursor, followed by rapid precipitation using tert-butanol antisolvent, in which process Ag nanoparticles were embedded into CACBB matrix (see Methods for details). Scanning electron microscope (SEM) images demonstrate that CACBB@Ag exhibited distinct morphological features and a reduced particle size compared to the original CACBB, suggesting that Ag nanoparticle incorporation influences the nucleation and growth of the perovskite phase (Figure S1). Notably, no Ag nanoparticles were found on the surface of CACBB@Ag, indicating their integration into the bulk perovskite structure. The spatial arrangement of Ag nanoparticles was characterized by transmission electron microscopy (TEM) (Figure 1a). The perovskite phase forms around the isolated Ag nanoparticles. The Ag nanoparticle region displayed a lattice spacing of 2.3 Å, consistent with the (111) crystal plane of Ag (Figure 1b). Energy-dispersive X-ray spectroscopy (EDS) mapping further corroborated the isolated nature of the Ag nanoparticles, with a distinct signal for Ag while Cs, Bi, Br, and Cu were uniformly distributed throughout the perovskite matrix (Figures 1c-h).

X-ray diffraction (XRD) patterns show that all peaks of CACBB@Ag are consistent with theoretical results for $Cs_2AgCuBiBr_6$ (Figure S2), with no additional peaks indicative of metallic Ag. This is likely due to the low Ag nanoparticle concentration (5 wt.%). A red-shift in the absorption spectrum is observed, along with a marked enhancement in visible-region absorption (Figure S3), resulting in a narrower bandgap of 2.09 eV. This shift is attributed to the LSPR effect of the embedded Ag nanoparticles. In fact, Ag nanoparticles have a wide absorption band and a strong absorption peak around 414 nm (Figure S4), corresponding to the LSPR band of Ag nanoparticles. X-ray photoelectron spectroscopy (XPS) analysis reveals Ag 3d peaks at 367.6 and 373.8 eV, consistent with Ag^+, similar to those observed in pristine CACBB (Figure 1i).[16a] No metallic Ag peaks are present. In contrast, CACBB/Ag, which was prepared by a two-step process and contains Ag nanoparticles on its surface, exhibits both Ag^+ and metallic Ag peaks at 368.2 and 374.1 eV.[19] This distinction supports the conclusion that Ag nanoparticles in CACBB@Ag are embedded within the perovskite matrix, as XPS is a surface-sensitive technique.

The Cu $2p_{3/2}$ peak at 932.0 eV indicates the predominant presence of Cu^+ in CACBB@Ag (Figure S5). Several weak satellite peaks are also observed at 955.8, 950.4, 943.2 and 938.8 eV, corresponding to Cu^{2+}.[16b] To investigate the exact position of Cu ions, we have performed ^{133}Cs and ^{209}Bi magic angel spinning solid-state nuclear magnetic resonance (MAS ssNMR) spectroscopy. The ^{133}Cs NMR spectrum reveals a symmetric peak at δ_{iso}= 84.32 ppm, confirming the presence of Cs^+ in

10.1002/anie.202424395

RESEARCH ARTICLE

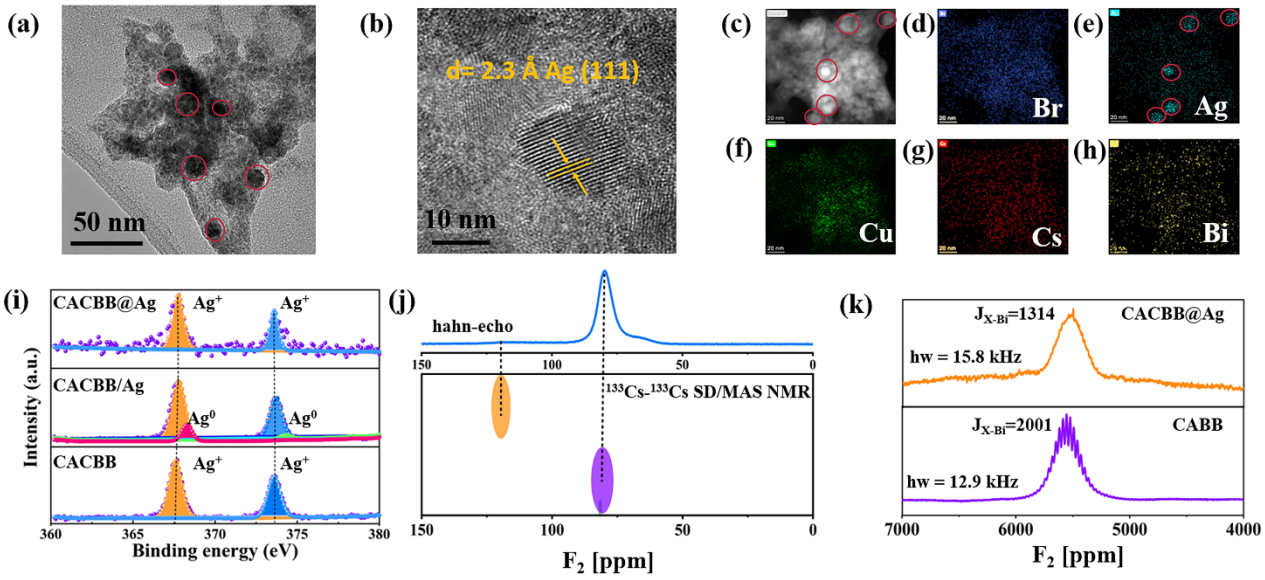

Figure 1 Morphology and structure characteristics of CACBB@Ag. (a) TEM, (b) HRTEM, and (c) HAADF-TEM images of CACBB@Ag, the elemental mapping images of CACBB@Ag for (d) Br, (e) Ag, (f) Cu, (g) Cs and (h) Bi. (i) Ag XPS spectra of CACBB, CACBB/Ag and CACBB@Ag samples. (j) The ^{133}Cs-^{133}Cs SD/MAS NMR and ^{133}Cs hahn-echo MAS NMR spectra of CACBB@Ag. (k) The ^{209}Bi ssNMR of CACBB@Ag and CABB.

CACBB@Ag (Figure 1j). A new peak at δ_{iso} = 125.53 ppm suggests Cu^{+}/Cu^{2+} ions are situated near Cs^{+} within the perovskite structure. The T_1 relaxation time, analyzed from saturation recovery curves through single-exponential functions (Figure S6), is notably shorter in CACBB@Ag (34.1 s) compared to pristine CABB (330 s). This faster relaxation is indicative of Cu^{2+} incorporation, which enhances electron spin coupling and facilitates nuclear relaxation.[20] This finding is corroborated by electron paramagnetic resonance (EPR) measurements (Figure S7). By further analyzing the ^{209}Bi MAS ssNMR spectra (Figure 1k), it was observed that the signal at δ_{iso} = 5500 ppm was significantly broaden in CACBB@Ag, further confirming the incorporation of Cu^{+}/Cu^{2+}. The observed spin-spin interaction (*J*-coupling) of $J_{Bi\text{-}X}$ in CACBB@Ag (1314 Hz, X: Br, Ag or Cu) is significantly lower than in $Cs_2AgBiBr_6$ (2001 Hz, X: Br or Ag), suggesting changes in the local bonding environment of Bi due to Cu^{+}/Cu^{2+} substitution.[21]

Photophysical properties

We systematically investigated the photophysical properties of CACBB@Ag through a series of experiments. The Raman spectra, presented in Figure 2a, reveal characteristic peaks at 60.3, 73.6, 135.7, 177.3, 360.6, and 518.2 cm^{-1} across all perovskite samples. Notably, both CACBB@Ag and CACBB/Ag exhibit substantial Raman enhancements relative to pristine CACBB. This enhancement is attributed to the local electromagnetic field induced by the plasmonic resonance of Ag nanoparticles.[22] Furthermore, the emission intensity of CACBB@Ag is markedly higher than that of CACBB/Ag, indicating a more efficient coupling of the Ag nanoparticles with the substrate, which maximizes the utilization of the plasmonic energy. To substantiate these findings, we performed finite-difference time-domain (FDTD) simulations to analyze the near-field distributions of isolated 15 nm Ag nanoparticles within CACBB@Ag and CACBB/Ag samples. Figure 2b illustrates the enhanced electromagnetic field near the Ag nanoparticles in both composites in the *xz* planes upon irradiation with 450 nm incident light along the z-axis. Notably, CACBB@Ag generates a more intense local field than CACBB/Ag, suggesting a stronger interaction between the embedded Ag nanoparticles and the perovskite substrate. This stronger coupling likely arises from the unique structural characteristics of CACBB@Ag, further verified by the improved optical absorption observed in CACBB@Ag (Figure S8). Then, the Kelvin probe force microscopy combined with surface photovoltage spectroscopy (KPFM-SPV) technique was applied to explore the dynamics of charge carriers. The SPV signal originates from the charge separation during diffusion process and its magnitude is proportional to the number of the photoexcited carriers undergoing separation.[23] As shown in Figure 2c, CACBB@Ag yields a significant higher SPV than CACBB and CACBB/Ag under SPR excitation, revealing that the more efficient separation of photoexcited carriers. The photoluminescence (PL) emission spectra depict that Ag nanoparticles is not detectable, which is consistent with the extremely low radiation efficiency of metal (Figure S4). However, in the presence of Ag nanoparticles, CACBB@Ag with a maximum broadband about at 650 nm exhibits a reduced intensity relative to other samples (Figure S9), meaning a more efficient suppression of electron-hole recombination facilitated by the embedded Ag nanoparticles. Additionally, the decreased semicircle in electrochemical impedance spectroscopy (EIS) signifies enhanced charge transfer kinetics at the interface between CACBB@Ag and the electrolyte (Figure S10).

To elucidate the mechanisms of photogenerated carrier dynamics and transfer, we performed transient absorption spectra (TAS) measurements. The ground-state bleach (GSB) of Ag (Figure 2d) and CACBB (Figure 2e) are observed at 414 and 578

10.1002/anie.202424395

RESEARCH ARTICLE

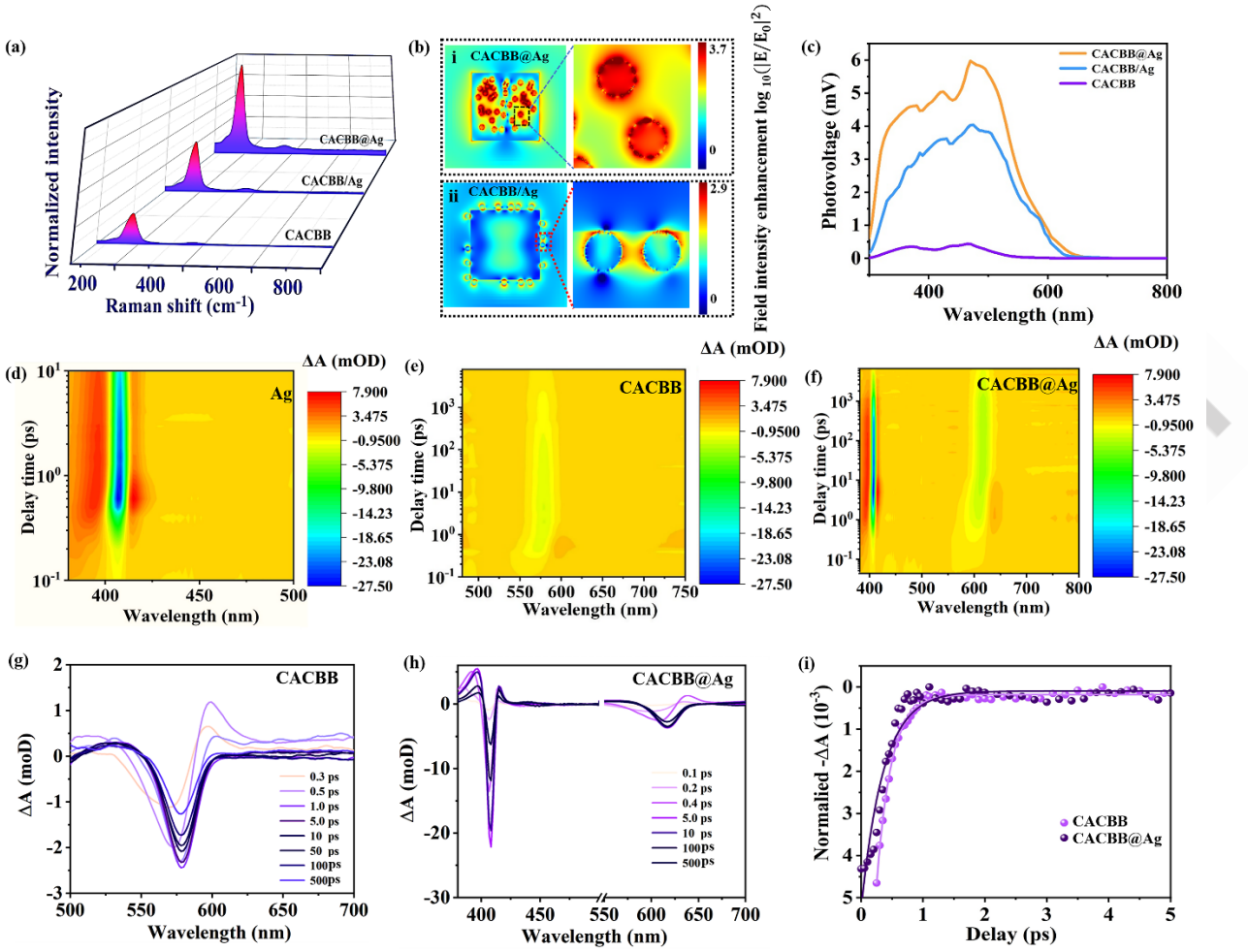

Figure 2 Photophysical properties of CACBB@Ag. (a) Raman spectra of CACBB, CACBB/Ag and CACBB@Ag. (b) The near-field distributions of (i) CACBB@Ag and (ii) CACBB/Ag by FDTD simulation at 450 nm excitation. The local field intensity in FDTD simulation is color coded by the scale bar on the right side of the panel. The dark red and dark blue colors represent the strongest and weakest enhancement effect, respectively. (c) Steady-state SPV spectra of CACBB, CACBB/Ag and CACBB@Ag photoanodes. Pseudo-color representation transient absorption spectra of (d) Ag nanoparticles, (e) CACBB and (f) CACBB@Ag. Transient absorption spectra of (g) CACBB and (h) CACBB@Ag excited by a 430 nm pump beam. (i) GSB dynamics probed at the band-edge for CACBB and CACBB@Ag with 430 nm excitation

nm, respectively. In sharp contrast, the GSB of the composite CACBB@Ag appeared at 614 nm (Figure 2f), suggesting that the embedded Ag nanoparticles modify the bandgap of CACBB. This observation is consistent with UV-Vis spectra (Figure S4), which further support the shift in the absorption edge for CACBB@Ag. In the visible region, both CACBB (Figure 2g) and CACBB@Ag (Figure 2h) exhibit prominent photoinduced absorption (PIA) signals, beginning at 600 nm and 640 nm, respectively. These PIA features are typically attributed to electron trapping states resulting from the separation of excited electrons into the conduction band after charge dissociation.[24] Notably, the positive PIA signals initially compete with the strong GSB signals as hot carriers undergo relaxation to lower energy states. This is followed by a gradual increase and eventual maximum of the GSB indicative of charge carriers migrating toward the energy band edge during thermalization and relaxation.[24]

The temporal evolution of these signals was further analyzed through biexponential decay fitting (Figure S11). The lifetime of plasmon-induced hot carriers in Ag nanoparticles was determined to be 9.84 ps, primarily influenced by electron-phonon scattering. In the CACBB@Ag composite, the carrier lifetime was reduced to 0.38 ps, demonstrating that the plasmonic Ag nanoparticles facilitate the transfer of hot carriers to the CACBB component for catalytic utilization. As for CACBB, hot carriers typically relax to the band edge within sub-ps timescales through carrier-phonon coupling. However, embedding Ag nanoparticles extended this relaxation time from 0.30 ps to 0.38 ps (Figure 2i), suggesting that the presence of Ag nanoparticles impedes the backward transfer of injected electrons and consequently prolongs the carrier lifetime. This effect enhances the overall photoelectric conversion efficiency by slowing down carrier relaxation and promoting more efficient charge transfer.

Photoelectrochemical synthesis of bromohydrins and H_2O_2

Photocatalytic activity evaluation was initially investigated by linear sweep voltammetry (LSV) in a three-electrode

10.1002/anie.202424395

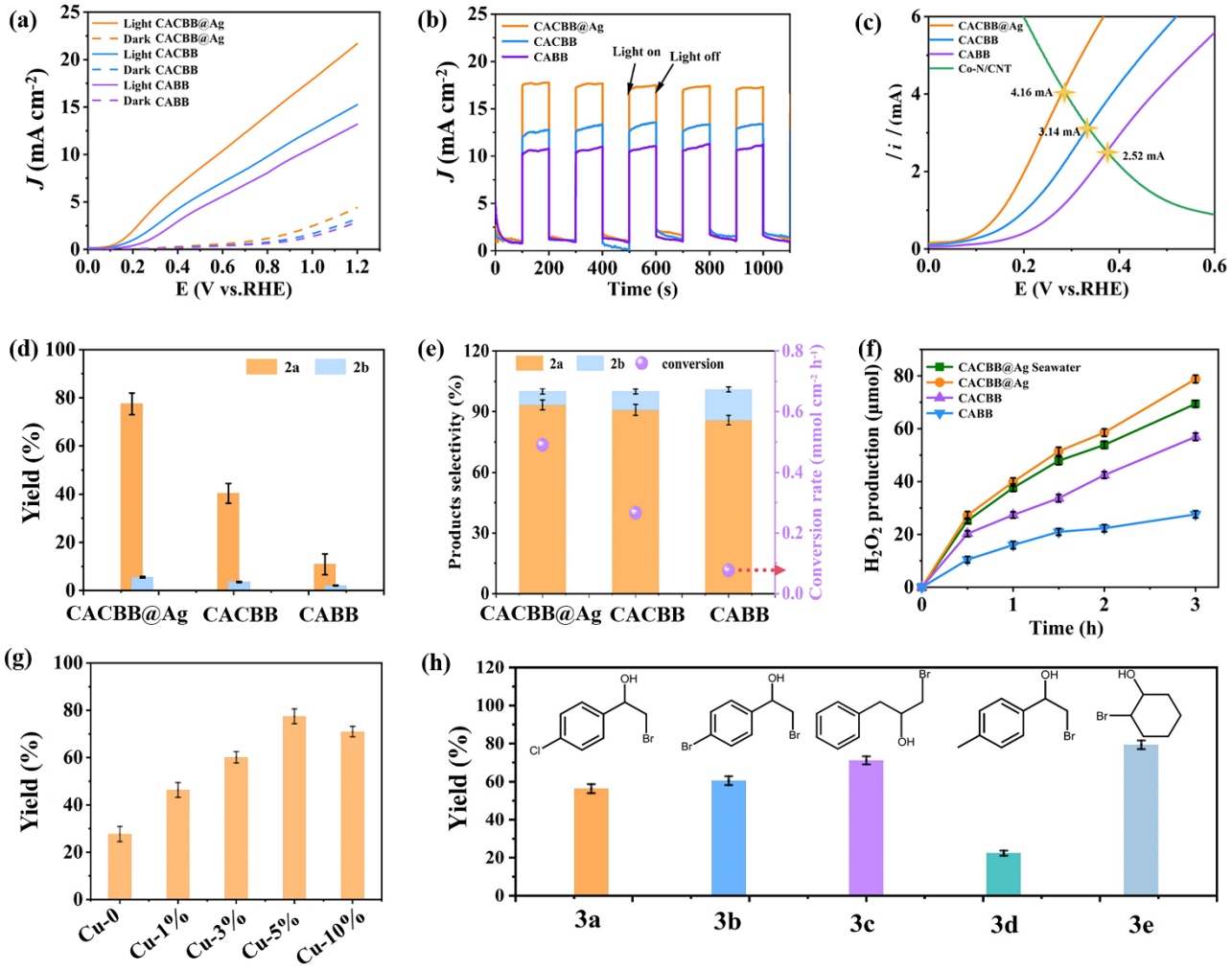

Figure 3 Photoelectrochemical synthesis of bromohydrins and H_2O_2. (a) LSV curves of different photoanodes under dark or light illumination (10 mV s^{-1}). (b) Photocurrent responses of CABB, CACBB and CACBB@Ag photoanodes under illumination at 1.08 (V vs. RHE). (c) The LSV overlapping of the different photoanodes and Co-N/CNT counter electrode. (d) The yield of 2-bromo-1-phenylethanol (**2a**) and 1,2-dibromoethane (**2b**) after photoelectrochemical reaction for 3 h. The photoelectrochemical reaction was performed in a sealed H-type cell. (e) The conversion rate of styrene and selectivity of **2a** and **2b** after photoelectrochemical reaction for 3 h. (f) H_2O_2 production during the photoelectrochemical reaction. (g) The yield of **2a** in photoelectrochemical cell assembled with CACBB@Ag containing different amount of Cu ions. (h) The yield of 1-(4-chlorophenyl) ethan-1-ol (**3a**), 2-bromo-1-(4-bromophenyl) ethan-1-ol (**3b**), 1-bromo-3-phenylpropane-2-alcohol (**3c**), 2-bromo-1-(p-tolyl) ethan-1-ol (**3d**) and 2-bromocyclohexan-1-ol (**3e**) in photoelectrochemical cell assembled with CACBB@Ag for 3 h. The photoelectrochemical measurements were repeated for four times.

photoelectrochemical cell (Figure 3a). The LSV curve of CABB and CACBB for Br^- oxidation exhibited current densities of 10.57 and 12.49 mA cm^{-2} at 1.08 V (versus RHE) under visible light irradiation (λ > 420 nm), respectively. Notably, the CACBB@Ag composite demonstrated an enhanced current density of 17.66 mA cm^{-2}, indicating a significant improvement in photocatalytic activity. Photocurrent responses recorded at 1.08 V are shown in Figure 3b. Upon visible light illumination, the photocurrent rapidly increased and stabilized at values of 17.57, 12.35, and 10.42 mA cm^{-2} for CACBB@Ag, CACBB, and CABB, respectively. This enhancement in photocurrent for CACBB@Ag suggests that the synergistic effect of SPR in Ag nanoparticles, combined with Cu ion doping in perovskite, significantly promotes Br^- oxidation. Subsequent photoelectrochemical reactions, involving styrene bromohydroxylation and H_2O_2 production, were conducted in an H-type two-compartment cell (Figure S12). The perovskite-based photoanode was immersed in Ar-saturated 1 M HBr solution with the dynamic equilibrium of dissolution-precipitation of perovskite, while the counter electrode was placed in an O_2-saturated 0.1 M NaPi buffer. LSV scans for Br^- oxidation, shown in Figure 3c, were recorded with the Co-N/CNT cathode for O_2 reduction. The CACBB@Ag photoanode exhibited an intersection point at 0.28 V (versus RHE) with a current of 4.16 mA, while CABB and CACBB displayed intersection points at 0.37 V (2.52 mA) and 0.33 V (3.14 mA), respectively. These results confirm that CACBB@Ag outperforms the other photoanodes, making it a superior candidate for the coupled synthesis of bromohydrins and H_2O_2.

The products of the photoanode cell reaction were analyzed using ^{1}H Nuclear Magnetic Resonance spectra (^{1}H NMR) and gas chromatography-mass spectrometry (GC-MS) (Figure S13). The reaction produced a mixture of 2-bromo-1-phenylethanol (**2a**) and its by-product, (1,2-dibromoethyl)-benzene (**2b**), as illustrated in Figure 3d. Notably, the CACBB@Ag photoanode yielded **2a** with

10.1002/anie.202424395

RESEARCH ARTICLE

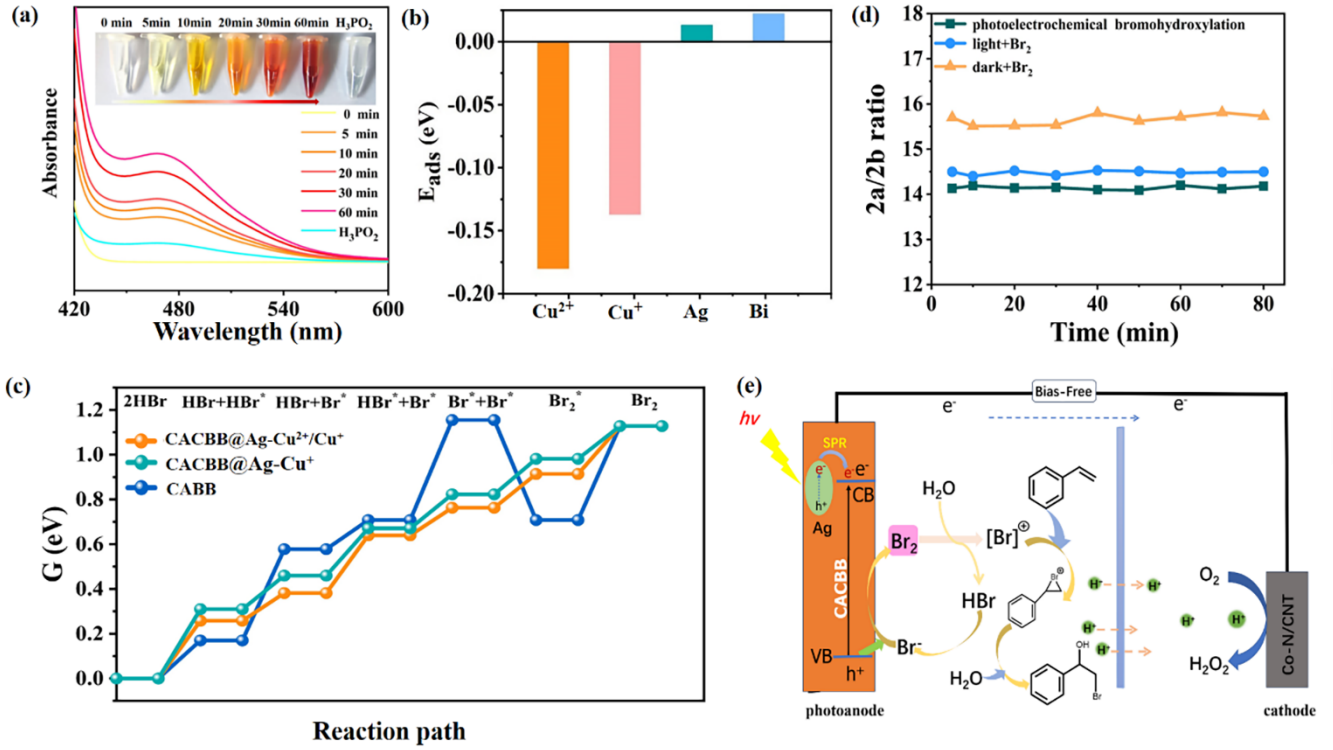

Figure 4 Mechanistic analysis of photoelectrochemical Bromohydroxylation. (a) UV-Vis spectra of the reaction solutions in the photoanode cell after photocatalytic reaction for different reaction times. (b) The adsorption energy of Br^- on Cu, Ag and Bi sites of the (004) plane of CACBB@Ag. (c) Gibbs free energy diagrams for Br^-oxidation over CABB and CACBB@Ag. (d) The yield ratio of **2a/2b** in different reaction environments, green symbol: photoelectrochemical bromohydroxylation of styrene in the sealed H-type cell under AM 1.5 G irradiation; blue symbol: the direct bromohydroxylation of styrene in Br_2-H_2O-styrene system under AM 1.5 G irradiation; yellow symbol: the direct bromohydroxylation of styrene in Br_2-H_2O-styrene system in dark. The photoelectrochemical measurements were repeated for three times. (e) Proposed formation mechanism for bias-free photoelectrochemical synthesis of **2a** over CACBB@Ag photoanode and H_2O_2 on cathode.

an efficiency of 77.5%, approximately 7 times higher than the yield obtained using CABB. The styrene conversion rate for the device with the CACBB photoanode was 0.27 mmol cm^{-2} h^{-1}, which was superior to the CABB-based device (0.076 mmol cm^{-2} h^{-1}). The CACBB@Ag photoanode demonstrated the highest catalytic performance, achieving a conversion rate of 0.49 mmol cm^{-2} h^{-1} and a selectivity of 93.4% for **2a** (Figure 3e). Furthermore, the device combining the CACBB@Ag photoanode with a Co-N/CNT cathode generated 77.4 μmol of H_2O_2 after 3 h operation (25.8 μmol h^{-1} cm^{-2}), surpassing the yields of the CABB-based (27.6 μmol) and CACBB-based (56.9 μmol) devices (Figure 3f). This performance exceeded that of previously reported bias-free photoelectrochemical systems (Table S1). Notably, when seawater was employed in the cathode cell, the CACBB@Ag-based device still produced 69.4 μmol of H_2O_2 after 3 h (22.8 μmol h^{-1} cm^{-2}), highlighting the potential of perovskite-based photoelectrochemical systems in seawater-related applications, such as uranium extraction or direct seawater fuel cell. [7a, b] We investigated the effect of Ag concentration on catalytic activity of CACBB@Ag. The results demonstrate that CACBB@Ag with 5 wt.% Ag nanoparticles exhibits an optimal catalytic performance. Compared to CACBB/Ag sample with surface-loaded Ag nanoparticles (5 wt.%), CACBB@Ag with embedded Ag nanoparticles show superior catalytic activity (Figure S14), indicating the critical role of the embedded plasmonic Ag in generating a high-intensity localized electromagnetic field. The role of Cu-doping in the CACBB@Ag photoanode for photoelectrochemical synthesis was also explored. Increasing the Cu-ion concentration led to enhanced product yields, with a 5% Cu-doping concentration providing the highest yield of both **2a** and H_2O_2 (Figure 3g; Figure S15). However, quantifying the influence of the Cu^+/Cu^{2+} ratio on catalytic activity remains complex due to experimental intricacies. The presence of Cu-induced sub-bandgap defects, indicated by a weak absorption tail at 859 nm in the UV-Vis spectrum (Figure S16), appears to enhance photoconductivity and carrier generation in the perovskite material.[25] Moreover, the doped samples exhibited reduced photoluminescence (PL) intensities compared to the pristine perovskite, suggesting that Cu-doping facilitates the dissociation of excitons via interactions with Cu 4s and 3d orbitals (Figure S17).[26] To confirm that the catalytic activity of the CACBB@Ag sample originates from its proposed composition and not from any degradation products of perovskite, several control experiments were conducted. No **2a** product and H_2O_2 were formed using blank fluorine-doped tin oxide (FTO) electrodes or FTO loaded with individual metal salt (CsBr, $CuBr_2$, $BiBr_3$ and AgBr) (Table S2). Additionally, mixing metal salts with $Cs_2AgCuBiBr_6$@Ag perovskite resulted in lower **2a** production, indicating that the catalytic activity is intrinsic to the perovskite material. The stability of the photoelectrochemical system was also evaluated over five continuous cycles. The yields of **2a** (Figure S18) and H_2O_2 (Figure S19) remained stable, indicating

10.1002/anie.202424395

the durability and sustained efficacy of the CACBB@Ag-based system over prolonged operation. The durability of CACBB@Ag is further validated through XRD, SEM, and TEM analyses (Figure S20 and Figure S21).

To illustrate the versatility of the photoelectrochemical bromohydroxylation of organic molecules with C=C bonds using the CACBB@Ag photoanode, a series of phenyl derivatives were evaluated, including 4-chlorophenylstyrene, 4-bromostyrene, allylbenzene, and 1-methyl-4-vinylbenzene (Figure 3h). The reaction of 4-chlorophenylstyrene led to the formation of 1-(4-chlorophenyl) ethan-1-ol (**3a**) with a yield of 56.3% (Figure S22). Similarly, the conversion of 4-bromostyrene produced 2-bromo-1-(4-bromophenyl) ethan-1-ol (**3b**) with a yield of 60.5% (Figure S23). Allylbenzene provided a notably higher yield of 71.2% for 1-bromo-3-phenylpropane-2-alcohol (**3c**) (Figure S24), attributed to the relatively weaker C=C bond in allylbenzene, which is more reactive to electrophilic attack compared to the conjugated C=C bonds in the aromatic ring.[27] In contrast, the reaction of 1-methyl-4-vinylbenzene afforded 2-bromo-1-(p-tolyl) ethan-1-ol (**3d**) with a reduced yield of 22.4% (Figure S25), likely due to the electron-donating effect of the methyl group, which diminishes the electrophilicity of the vinyl group. Furthermore, the nonpolar cyclohexene molecule was tested in the system, yielding 2-bromocyclohexan-1-ol (**3e**) with a high yield of 79.4% (Figure S26). This result is attributed to the less-conjugated nature of the C=C bond in cyclohexene, which makes it more susceptible to electrophilic addition.[28] In contrast, the C=C bonds in styrene are part of a conjugated system with the benzene ring, where the π-electron delocalization through resonance reduces their reactivity.[29] The amount of H_2O_2 produced at the cathode was found to be nearly independent of the substrate used in the anode, with H_2O_2 levels ranging from 77.6 to 78.9 μmol (Figure S27). This indicates that the formation of H_2O_2 is not influenced by efficiency of the bromohydroxylation reaction, further demonstrating the robustness and general applicability of the photoelectrochemical bromohydroxylation strategy.

Mechanistic studies of photoelectrochemical Bromohydroxylation

We explored the formation pathway of bromohydrins in photoelectrochemical system using styrene as the substrate. Without the addition of styrene, we found that the solution color in photoanode cell transformed gradually from colorless to dark red with the progression of light irradiation, with the UV-Vis spectra revealing an increasing absorption intensity centered at 476 nm (Figure 4a). When H_3PO_2 was added into the reaction system, the resulting dark red solution translated into colorless under irradiation since H_3PO_2 is a strong reductant for the reduction of Br_2 into Br^-, and the absorption peak at 476 nm disappeared immediately. These results imply the formation of Br_2 from Br^- oxidation. Although the valence band potential of CACBB@Ag is thermodynamically favorable for the four-electron water oxidation, no O_2 bubbles were observed in the sealed photoanode cell, demonstrating that of the two-electron Br^- oxidation in saturated HBr solution can sufficiently suppress the competing water oxidation over CACBB@Ag photoanode. To illuminate the superior catalytic ability of CACBB@Ag on catalyzing Br^- oxidation reaction, we further conducted the spin-polarized density functional theory (DFT) calculations to comprehend the active centers and reveal the underlying mechanism. The detailed computational information is given in the Methods section. The calculations showed that the adsorption energy of Br^- on the Ag site and Bi site on the (004) plane of CACBB@Ag is 0.023 and 0.042 eV, respectively, which is comparable with that on the (004) plane of CABB (Figure S28). By contrast, Br^- exhibits a lower adsorption energy of -0.13 and -0.18 eV on the Cu^+ site and Cu^{2+} site (close to an Ag vacancy) of CACBB@Ag (004) plane, respectively, indicating thermodynamically favorable interactions (Figure 4b). The increase in adsorption energy with the oxidation state of the active site suggests that Cu^{2+} enhances Br^- oxidation, likely due to the stronger electrostatic interaction between Cu^{2+} and Br^- compared to Cu^+. This is consistent with the Sabatier principle, which posits that weak adsorption correlates with slower reaction kinetics.[30] Therefore, Cu sites in CACBB are more conducive to Br^- oxidation, optimizing the balance between the catalyst and the reactant. Further, Gibbs free energy diagrams for Br^- oxidation reveal that Br^- adsorbs onto the Cu^{2+} site of CACBB@Ag to form Br^{-}* (* represents the reaction site), which is then oxidized to Br* by a photogenerated hole, with a reaction energy barrier of 0.12 eV. For comparison, the reaction barriers for Br^- oxidation on the Ag site of CABB and the Cu^+ site of CACBB@Ag are 0.45 and 0.15 eV, respectively, both higher than that on the Cu^{2+} site of CACBB@Ag (Figure 4c). Subsequently, the two Br* species combine to produce Br_2*. The formation of Br_2* at the Cu^{2+} and Cu^+ sites exhibit reaction energy barriers of 0.13 eV and 0.16 eV, respectively. These results demonstrate that Cu^{2+} reduces the activation energy of the rate-determining step, promoting the oxidation of Br^- over CACBB@Ag.

To further reveal the formation processes of bromohydrins, we have performed several control experiments. In LSV measurement, the photocurrent response for Br^- oxidation was nearly unchanged when styrene substrate was added into the reaction solution, verifying that the formation of **2a** from styrene proceeded in the bulk solution rather than on perovskite surface (Figure S29). The bromohydroxylation of styrene was then examined using Br_2 as the reactant in aqueous solution under light irradiation or in dark. The yield ratio of **2a** and **2b** was 15.8 with **2a** as the main product owing to the electrophilic addition mechanism (Figure 4d). No radicals were detected in the solution (Figure S30). Under light irradiation, the yield ratio of **2a** and **2b** was slightly decreased to 14.6, which is similar with that in the photoelectrochemical system (the yield ratio of **2a** and **2b** is 14.0) (Figure 4d). Moreover, Br• and carbon-centered radicals were detected and no •OH was observed after 5 min illumination, while the continuous irradiation resulted in the disappearance of Br• and the weakening of the carbon radical (Figure S30). These results mean that Br• would interact with C-H bond to produce a carbon-centered radical, which then yields **2b**. These results indicates that the formation of **2a** and **2b** mainly originates from the electrophilic addition and the radical addition mechanism, respectively. $H_2{}^{18}O$ isotopic labelling experiments were subsequently conducted to explore the origin of oxygen of **2a**. When $H_2{}^{18}O$ were employed to dilute the concentrated HBr stock solution, the product **2a** showed significant ion peaks at the mass-

to-charge ratio (m/z) of 203.8 and 201.8 (Figure S31), indicating that H_2O is the source of oxygen in **2a**. Based on the experimental and theoretical results, the proposed pathway for photoelectrochemical bromohydrins and H_2O_2 production is illustrated in Figure 4e, which simultaneously comprises the successive surface and solution reaction processes in photoelectrode cell. Under visible light irradiation, Ag nanoparticles and CACBB nanoparticles in CACBB@Ag can be excited to generate surface plasmons and electron/hole pairs, respectively. Once formed, the surface plasmons decay rapidly and generate a large number of high-energy electrons. Afterwards, a considerable number of these plasmon-induced electrons are delivered to the conduction band of CACBB, which are then transferred to the counter electrode for the two-electron reduction of O_2 into H_2O_2. In photoanode cell, Br^- is oxidized into Br_2 at the photoanode surface by photogenerated holes, and then Br_2 is disproportionated to $[Br]^+$ (HOBr) and HBr in the aqueous solution. According to the electrophilic addition rules for olefins,[31] $[Br]^+$ as electrophilic reagent interacts with the π electrons of the C=C double bond to form cyclobromination intermediate, which subsequently experiences the attack of water and yields **2a**.

Conclusion

In summary, we report the incorporation of Cu^+/Cu^{2+} into $Cs_2AgBiBr_6$ perovskite and the integration of plasmonic Ag nanoparticles to enhance the photoelectrochemical synthesis of bromohydrins and H_2O_2. The embedded Ag nanoparticles generate localized and intense electromagnetic fields that facilitate the generation and separation of charge carriers in the photoanode. Our experimental results, complemented by DFT calculations, reveal that the partial substitution of Ag^+ by Cu^+/Cu^{2+} not only promotes charge separation but also significantly accelerates the oxidation of Br^-. The bromhydroxylation reaction proceeds through an electrophilic addition mechanism, with water serving as the oxygen donor. The synergistic effects of Cu ion substitution and plasmonic Ag nanoparticles result in a remarkable 7-fold increase in the yield of 2-bromo-1-phenylethanol and an impressive H_2O_2 productivity of 25.8 μmol h^{-1} cm^{-2}, offering promising potential for future large-scale, efficient photoelectrochemical processes in both organic and inorganic chemical synthesis.

Supporting Information

The authors have cited additional references within the Supporting Information. [32-37]

Acknowledgements

This work was financially supported by National Natural Science Foundation of China (52172195) and Hainan Science and Technology Major Project (ZDKJ2020011). Partial support from the Robert A. Welch Foundation (B-0027) (S. M.) and Saudi Water Authority through Energy Innovation Research Chair at Princess Nourah bint Abdulrahman University (T.A.) is also acknowledged.

Keywords: Photosynthesis, Perovskite, Bromohydroxylation, Hydrogen peroxide

References

[1] M. G. Sendeku, T. A. Shifa, F. T. Dajan, K. B. Ibrahim, B. Wu, Y. Yang, E. Moretti, A. Vomiero, F. Wang, *Adv. Mater.* **2024**, 36, 2308101.

[2] a) L. Huang, P. Wang, Y. Jiang, K. Davey, Y. Zheng, S. Z. Qiao, *J. Am. Chem. Soc.* **2023**, 145, 15565-15571; b) Y. Ashikari, A. Shimizu, T. Nokami, J. i. Yoshida, *J. Am. Chem. Soc.* **2013**, 135, 16070-16073; c) C.X. Ye, Y. Y. Melcamu, H.H. Li, J. T. Cheng, T.T. Zhang, Y. P. Ruan, X. Zheng, X. Lu, P. Q. Huang, *Nat. Commun.* **2018**, 9, 410; d) D. E. Holst, D. J. Wang, M. J. Kim, I. A. Guzei, Z. K. Wickens, *Nature* **2021**, 596, 74-79.

[3] a) Y. M. Cao, D. Lentz, M. Christmann, *J. Am. Chem. Soc.* **2018**, 140, 10677-10681; b) J. Kim, X. Sun, B. A. van der Worp, T. Ritter, *Nat. Catal.* **2023**, 6, 196-203.

[4] a) A. Podgoršek, M. Zupan, J. Iskra, *Angew. Chem. Int. Ed.* **2009**, 48, 8424-8450; b) Z. Chen, *Coord. Chem. Rev.* **2022**, 457, 214404.

[5] a) J. J. Dong, E. Fernández-Fueyo, J. Li, Z. Guo, R. Renirie, R. Wever, F. Hollmann, *Chem. Commun*. **2017**, 53, 6207-6210; b) J. N. Carter-Franklin, J. D. Parrish, R. A. Tschirret-Guth, R. D. Little, A. Butler, *J. Am. Chem. Soc.* **2003**, 125, 3688-3689.

[6] a) L. Li, X. Huo, S. Chen, Q. Luo, W. Wang, Y. Wang, N. Wang, *Small* **2023**, 19, 2301865; b) W. Wang, Q. Song, Q. Luo, L. Li, X. Huo, S. Chen, J. Li, Y. Li, S. Shi, Y. Yuan, X. Du, K. Zhang, N. Wang, *Nat. Commun.* **2023**, 14, 2493.

[7] a) K. Mase, M. Yoneda, Y. Yamada, S. Fukuzumi, *Nat. Commun.* **2016**, 7, 11470.b) Y. Cai, Y. Zhang, Z. Lv, S. Zhang, F. Gao, M. Fang, M. Kong, P. Liu, X. Tan, B. Hu, X. Wang, *Appl. Catal. B: Environ*. **2022**, 310, 121343. c) D. Tan, R. Zhuang, R. Chen, M. Ban, W. Feng, F. Xu, X. Chen, Q. Wang, *Adv. Funct. Mater*. **2024**, 34, 2311655.

[8] a) Z. Li, L. Luo, M. Li, W. Chen, Y. Liu, J. Yang, S. M. Xu, H. Zhou, L. Ma, M. Xu, X. Kong, H. Duan, *Nat. Commun.* **2021**, 12, 6698; b) T. Li, T. Kasahara, J. He, K. E. Dettelbach, G. M. Sammis, C. P. Berlinguette, *Nat. Commun.* **2017**, 8, 390.

[9] a) J. Kim, J. Jang, T. Hilberath, F. Hollmann, C. B. Park, *Nat. Synth.* **2022**, 1, 776-786; b) D. Liu, J. C. Liu, W. Cai, J. Ma, H. B. Yang, H. Xiao, J. Li, Y. Xiong, Y. Huang, B. Liu, *Nat. Commun.* **2019**, 10, 1779.

[10] a) M. V. Kovalenko, L. Protesescu, M. I. Bodnarchuk, *Science* **2017**, 358, 745-750; b) S. Chen, C. Wu, B. Han, Z. Liu, Z. Mi, W. Hao, J. Zhao, X. Wang, Q. Zhang, K. Liu, J. Qi, J. Cao, J. Feng, D. Yu, J. Li, P. Gao, *Nat. Commun.* **2021**, 12, 5516.

[11] a) S. Park, W. J. Chang, C. W. Lee, S. Park, H. Y. Ahn, K. T. Nam, *Nat. Energy* **2016**, 2; b) C. Geng, S. Xu, H. Zhong, A. L. Rogach, W. Bi, *Angew. Chem. Int. Ed.* **2018**, 57, 9650-9654.

[12] a) Y. Rong, X. Hou, Y. Hu, A. Mei, L. Liu, P. Wang, H. Han, *Nat. Commun.* **2017**, 8, 14555; b) S. Chen, H. Yin, P. Liu, Y. Wang, H. Zhao, *Adv. Mater.* **2023**, 35, 2203836.

[13] a) H. Lei, D. Hardy, F. Gao, *Adv. Funct. Mater.* **2021**, 31, 2105898; b) Q. Li, Y. Wang, W. Pan, W. Yang, B. Zou, J. Tang, Z. Quan, *Angew. Chem. Int. Ed.* **2017**, 56, 15969-15973; c) Z. Zhang, Y. Liang, H. Huang, X. Liu, Q. Li, L. Chen, D. Xu, *Angew. Chem. Int. Ed.* **2019**, 58, 7263-7267.

10.1002/anie.202424395

[14] a) J. Wang, M. Zhang, Z. Chen, L. Li, G. Jiang, Z. Li, *ACS Energy Lett.* **2024**, 9, 653-661; b) Z. Zhang, Q. Sun, Y. Lu, F. Lu, X. Mu, S. H. Wei, M. Sui, *Nat. Commun.* **2022**, 13, 3397.

[15] a) M. Keshavarz, E. Debroye, M. Ottesen, C. Martin, H. Zhang, E. Fron, R. Küchler, J. A. Steele, M. Bremholm, J. Van de Vondel, H. I. Wang, M. Bonn, M. B. J. Roeffaers, S. Wiedmann, J. Hofkens, *Adv. Mater.* **2020**, 32, 2001878; b) H. J. Jöbsis, K. Fykouras, J. W. C. Reinders, J. van Katwijk, J. M. Dorresteijn, T. Arens, I. Vollmer, L. A. Muscarella, L. Leppert, E. M. Hutter, *Adv. Funct. Mater.* **2023**, 2306106.

[16] a) F. Ji, Y. Huang, F. Wang, L. Kobera, F. Xie, J. Klarbring, S. Abbrent, J. Brus, C. Yin, S. I. Simak, I. A. Abrikosov, I. A. Buyanova, W. M. Chen, F. Gao, *Adv. Funct. Mate.* **2020**, 30; b) G. Liu, Z. Zhang, C. Wu, Y. Zhang, X. Li, W. Yu, G. Yao, S. Liu, J. j. Shi, K. Liu, Z. Chen, L. Xiao, B. Qu, *Adv. Funct. Mate.* **2021**, 32; c) F. Locardi, M. Cirignano, D. Baranov, Z. Dang, M. Prato, F. Drago, M. Ferretti, V. Pinchetti, M. Fanciulli, S. Brovelli, L. De Trizio, L. Manna, *J. Am. Chem. Soc*. **2018**, 140, 12989-12995.; d) Q. Zhang, S. Liu, M. He, W. Zheng, Q. Wan, M. Liu, X. Liao, W. Zhan, C. Yuan, J. Liu, H. Xie, X. Guo, L. Kong, L. Li, *Angew. Chem. Int. Ed.* **2022**, 61, e202205463; e) W. Mihalyi-Koch, G. Folpini, C. R. Roy, W. Kaiser, C. S. Wu, K. M. Sanders, I. A. Guzei, J. C. Wright, F. De Angelis, D. Cortecchia, A. Petrozza, S. Jin, *J. Am. Chem. Soc.* **2023**, 145, 28111-28123.

[17] a) X. Huang, H. Li, C. Zhang, S. Tan, Z. Chen, L. Chen, Z. Lu, X. Wang, M. Xiao, *Nat. Commun.* **2019**, 10, 1163; b) Y. Kim, J. G. Smith, P. K. Jain, *Nat. Chem.* **2018**, 10, 763-769; c) S. Linic, P. Christopher, D. B. Ingram, *Nat. Mater.* **2011**, 10, 911-921.

[18] a) S. K. Cushing, J. Li, F. Meng, T. R. Senty, S. Suri, M. Zhi, M. Li, A. D. Bristow, N. Wu, *J. Am. Chem. Soc.* **2012**, 134, 15033-15041; b) Y. Wang, Y. Li, X. Yang, T. Wang, X. Du, A. Zhu, W. Xie, W. Xie, *Angew. Chem. Int. Ed.* **2024**, 63, e202318817; c) D. B. Ingram, S. Linic, J. *Am. Chem. Soc.* **2011**, 133, 5202-5205; d) C. Boerigter, R. Campana, M. Morabito, S. Linic, *Nat. Commun.* **2016**, 7, 10545.

[19] Y. Ren, C. Li, Q. Xu, J. Yan, Y. Li, P. Yuan, H. Xia, C. Niu, X. Yang, Y. Jia, *Appl. Catal. B: Environ.* **2019**, 245, 648-655.

[20] D. J. Kubicki, D. Prochowicz, A. Pinon, G. Stevanato, A. Hofstetter, S. M. Zakeeruddin, M. Grätzel, L. Emsley, *J. Mater. Chem. A* **2019**, 7, 2326-2333.

[21] L. Kobera, S. A. Southern, J. M. Frost, D. L. Bryce, *Solid State Nucl. Magn. Reson.* **2017**, 84, 20-27.

[22] J. Reguera, J. Langer, D. Jiménez de Aberasturi, L. M. Liz-Marzán, *Chem. Soc. Rev.* **2017**, 46, 3866-3885.

[23] R. Chen, Z. Ren, Y. Liang, G. Zhang, T. Dittrich, R. Liu, Y. Liu, Y. Zhao, S. Pang, H. An, C. Ni, P. Zhou, K. Han, F. Fan, C. Li, *Nature* **2022**, 610, 296-301.

[24] J. Chen, M. E. Messing, K. Zheng, T. Pullerits, *J. Am. Chem. Soc.* **2019**, 141, 3532-3540.

[25] N. Kumar Tailor, S. Singh, M. A. Afroz, K. K. Pant, S. Satapathi, *Appl. Catal. B: Environ.* **2024**, 340, 123247.

[26] Y. Li, Y. Gao, Z. Deng, Y. Cao, T. Wang, Y. Wang, C. Zhang, M. Yuan, W. Xie, *Nat. Commun.* **2023**, 14, 4673.

[27] T. Q. Li, J. Y. Tan, W. Deng, Z. Y. Xu, *Dalton Trans.* **2020**, 49, 17395-17400.

[28] J. Mehara, M. Anania, P. Kočovský, J. Roithová, *ACS Catal.* **2024**, 14, 5710-5719.

[29] L. Reuter, A. Lüchow, *Nat. Commun.* **2021**, 12, 4820.

[30] A. J. Medford, A. Vojvodic, J. S. Hummelshøj, J. Voss, F. Abild-Pedersen, F. Studt, T. Bligaard, A. Nilsson, J. K. Nørskov, *J Catal.* **2015**, 328, 36-42.

[31] X. Liu, Z. Chen, S. Xu, G. Liu, Y. Zhu, X. Yu, L. Sun, F. Li, *J. Am. Chem. Soc*. **2022**, 144, 19770-19777.

[32] K. Mase, M. Yoneda, Y. Yamada, S. Fukuzumi, *ACS Energy Lett.* **2016**, 1, 913-919.

[33] K. Mase, M. Yoneda, Y. Yamada, S. Fukuzumi, *Nat. Commun.* **2016**, 7, 11470.

[34] K. Fuku, Y. Miyase, Y. Miseki, T. Funaki, T. Gunji, K. Sayama, *Chem Asian J.* **2017**, 12, 1111-1119.

[35] M. Ko, L. T. M. Pham, Y. J. Sa, J. Woo, T. V. T. Nguyen, J. H. Kim, D. Oh, P. Sharma, J. Ryu, T. J. Shin, S. H. Joo, Y. H. Kim, J. W. Jang, *Nat. Commun.***2019**, 10, 5123.

[36] T. H. Jeon, H. Kim, H. i. Kim, W. Choi, *Energy Environ. Sci.* **2020**, 13, 1730-1742.

[37] T. H. Jeon, B. Kim, C. Kim, C. Xia, H. Wang, P. J. J. Alvarez, W. Choi, *Energy Environ. Sci.* **2021**, 14, 3110-3119.

10.1002/anie.202424395

Entry for the Table of Contents

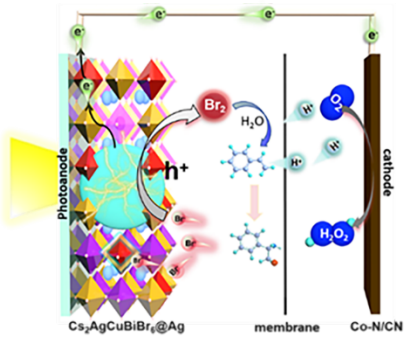

Lead-free $Cs_2AgCuBiBr_6$ perovskite with body-embedded Ag nanoparticles synergistically improve the utilization efficiency of photogenerated carrier and the adsorption and oxidation of Br^-, ensuring the high-efficiency synthesis of bromohydrins and H_2O_2 in an unbiased photoelectrochemical system.